

Electronic Supplementary Information (ESI) for

**Formation and local conduction of nanopits in BiFeO₃
epitaxial films**

Yajuan Zhao, Zhigang Yin, Xingwang Zhang,* Zhen Fu, and Jinliang Wu*

*Key Lab of Semiconductor Materials Science, Institute of Semiconductors, Chinese
Academy of Sciences, Beijing, 100083, P. R. China*

*Corresponding author. E-mail: yzhg@semi.ac.cn and xwzhang@semi.ac.cn

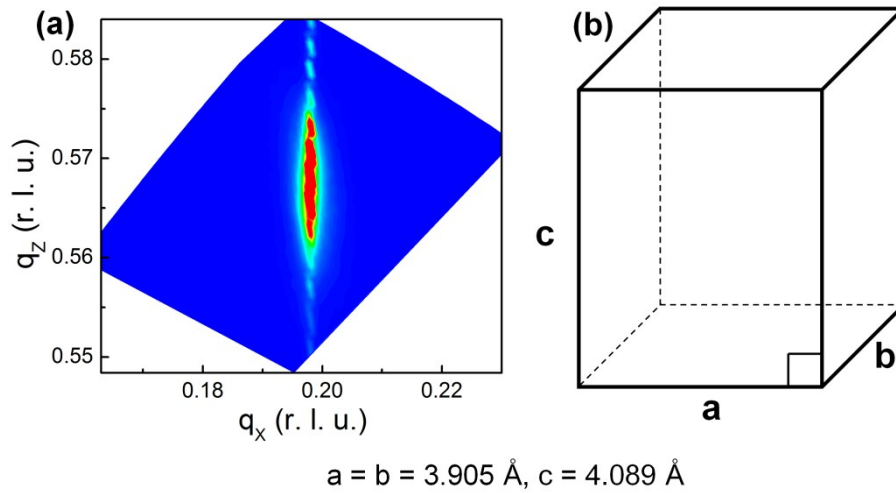


Fig. S1 (a) RSM collected around (103) reflection of the 10-nm-thick BFO film; no notable splitting was found, suggesting a tetragonal symmetry rather than the commonly observed M_A structure. (b) Schematic illustration of the crystal structure of the 10-nm-thick BFO film derived from (a).

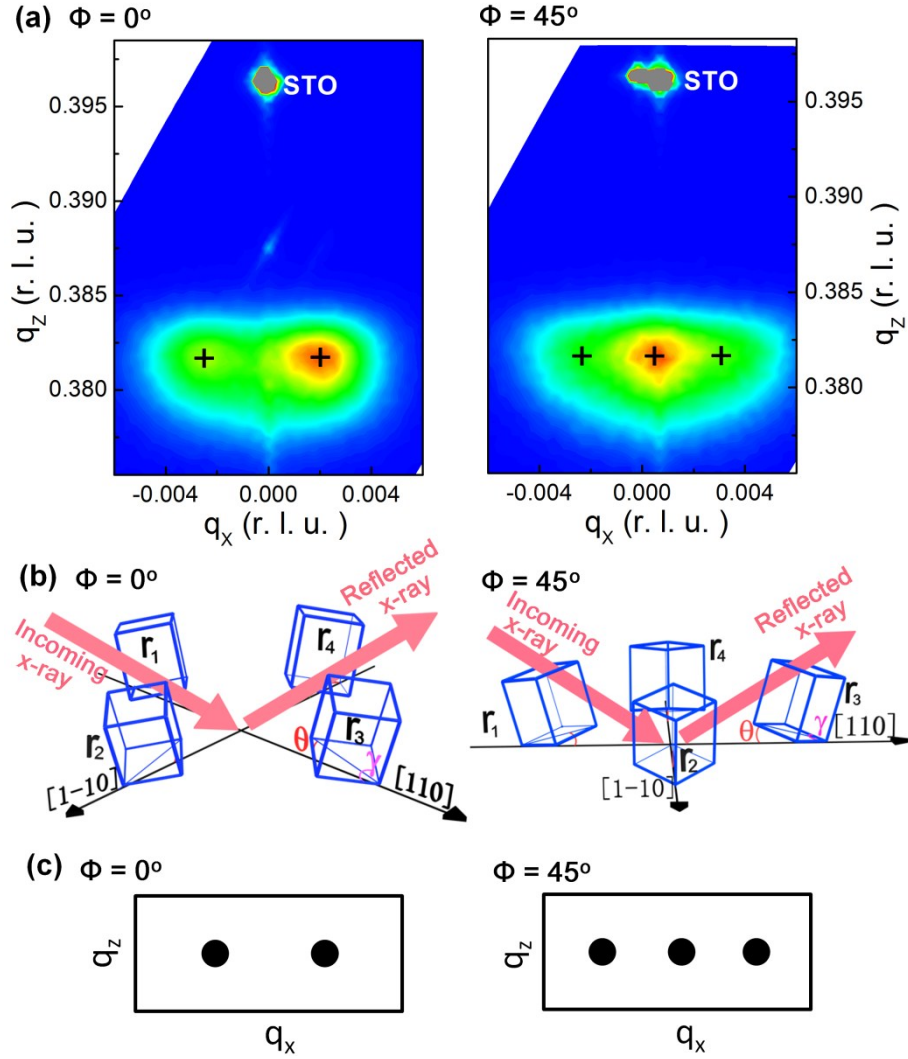


Fig. S2 (a) (002) RSMs measured at $\Phi = 0^\circ$ and $\Phi = 45^\circ$ for the 270-nm-thick BFO/Nb:STO(001) film; Φ denotes the angle between the $[100]$ axis of Nb:STO and the projection of the incident x-ray on the Nb:STO(001) plane. (b) The domain variants, labeled as r_1, r_2, r_3 and r_4 , under measuring configurations of $\Phi = 0^\circ$ and $\Phi = 45^\circ$. (c) Representations of the (002) plane of the BFO in the reciprocal space, under measuring configurations of $\Phi = 0^\circ$ and $\Phi = 45^\circ$.

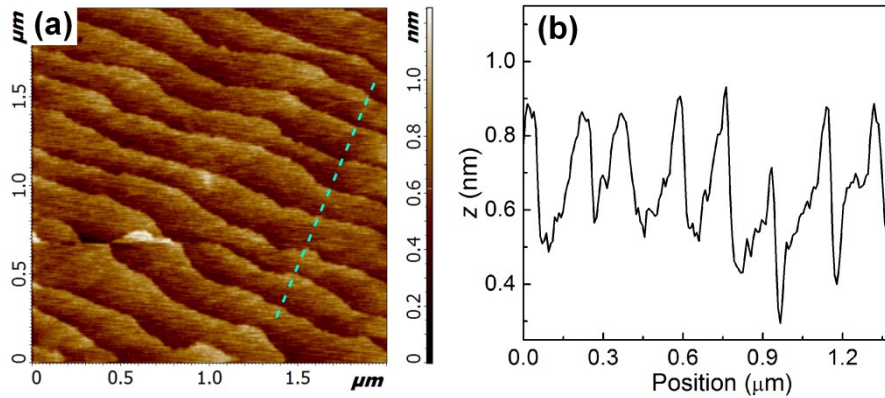


Fig. S3 (a) Typical AFM morphology of the Nb:STO substrate prepared by HF-buffer etching and subsequent oxygen annealing at 1000 °C. (b) The line trace collected along the dashed line in (a), which reveals an atomically smooth, terrace-step surface.

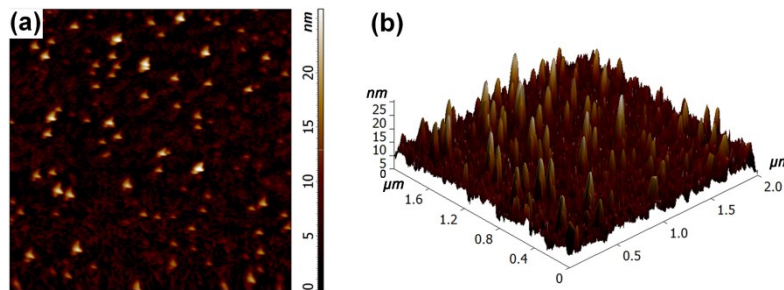


Fig. S4 (a) Top view and (b) tilted view of the surface morphology of the 30-nm-thick BFO film deposited on STO(111) substrate. The scan area is $2 \times 2 \mu\text{m}^2$.

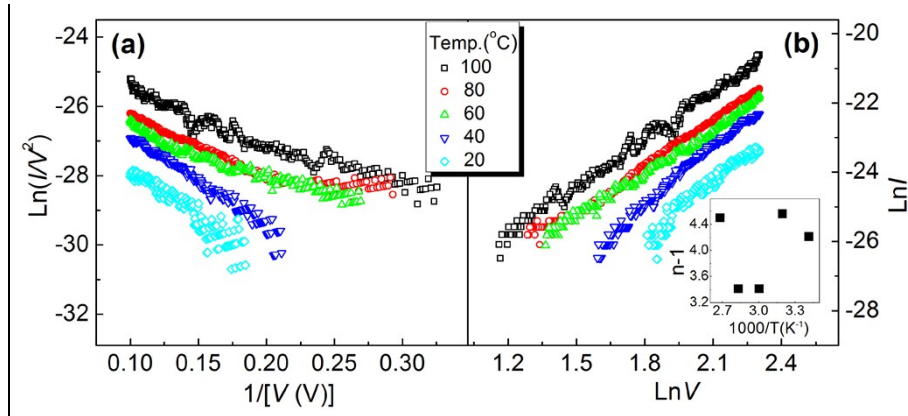


Fig. S5 (a) $\ln(I/V^2)$ versus $1/V$ plots of the I - V curves; a strong temperature-dependence of the data was observed, in contradictory with the FN tunneling mechanism. (b) The dependence of I on V^n with $(n-1)$ versus T^{-1} shown in the inset; for $n > 2$, a linear relationship between $(n-1)$ and T^{-1} , which is absent in our data, is expected under the frame of SCL conduction.

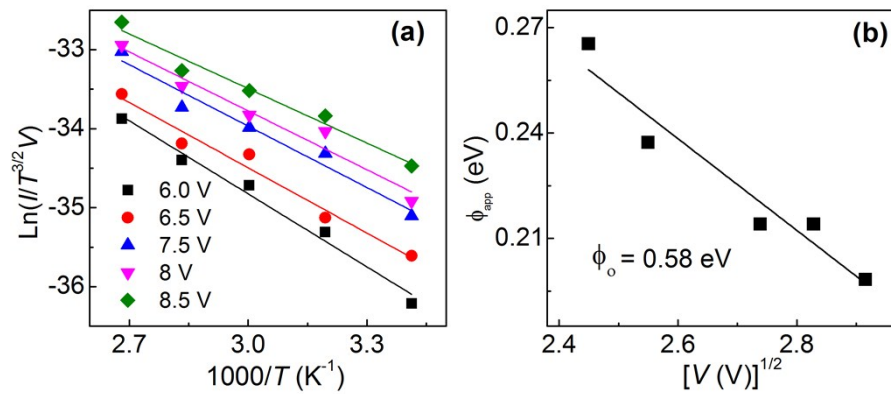


Fig. S6 (a) $\ln(I/T^{3/2}V)$ versus $1/T$ plots for various voltages; the linear fits of these data yield the values of Φ_{app} . (b) The dependence of Φ_{app} on $V^{1/2}$; extrapolating the linear relationship between Φ_{app} and $V^{1/2}$ gives rise to a Schottky barrier height of 0.58 eV.

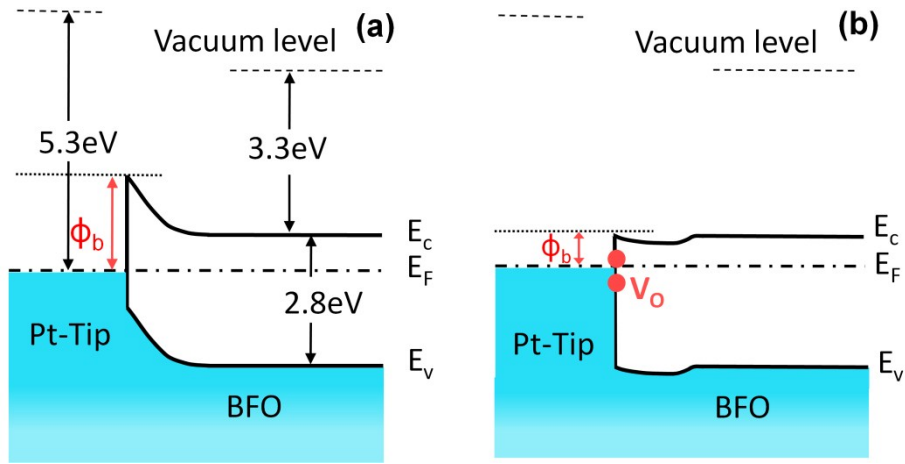


Fig. S7 Band alignments of the Pt/BFO nanopit interface without (a) and with (b) oxygen vacancies, by taking into account the work function of Pt, as well as the electron affinity and bandgap values of BFO. The appearance of oxygen vacancies on the BFO nanopit surface significantly reduces the Schottky barrier height, defined by Φ_b , and therefore results in a novel interface-regulated PF conduction of the Pt-tip/BFO-nanopit junction.

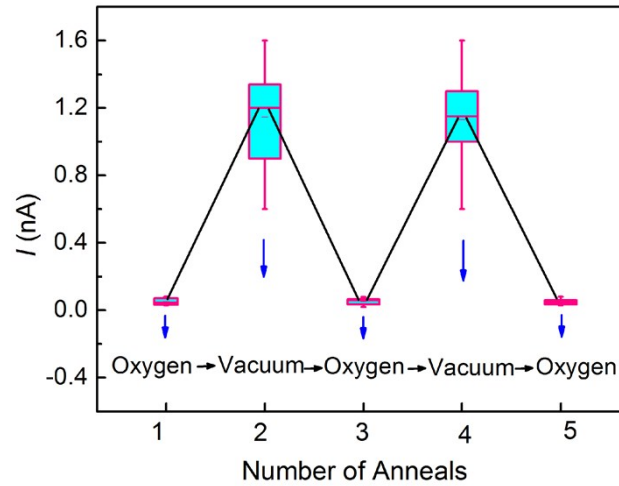


Fig. S8 Variation of local current collected within the nanopits with sequentially annealing in oxygen atmosphere and in vacuum for the 150-nm-thick BFO shown as box plots. The statistical data for each anneal were collected from more than 15 nanopits.

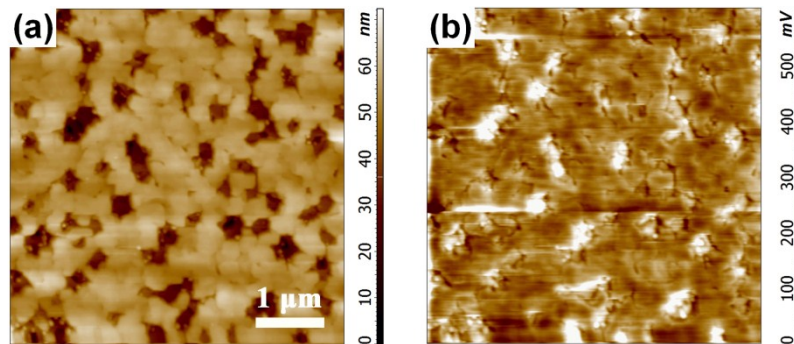


Fig. S9 (a) Morphology and (b) KPFM image of the 150-nm-thick BFO film. The scan area is $5 \times 5 \mu\text{m}^2$.